Arabian Journal of Chemistry (2022) **15**, 103513

King Saud University

Arabian Journal of Chemistry

www.ksu.edu.sa
www.sciencedirect.com

ORIGINAL ARTICLE

Facile synthesis of Z-scheme NiO/α-MoO_3 p-n heterojunction for improved photocatalytic activity towards degradation of methylene blue

Jintao Li [a,b], Hongjie Liu [c], Zhuo Liu [a], Daiqiong Yang [b], Mengzhao Zhang [b], Luning Gao [b], Yahong Zhou [b], Changyu Lu [a,b,*]

[a] *Experimental Practising & Teaching Center, Hebei GEO University, Shijiazhuang 050031, PR China*
[b] *Hebei Province Key Laboratory of Sustained Utilization & Development of Water Recourse, Hebei Province Collaborative Innovation Center for Sustainable Utilization of Water Resources and Optimization of Industrial Structure, School of Water Resource and Environment, Hebei Geo University, Shijiazhuang 050031, PR China*
[c] *School of Chemistry and Chemical Engineering, Guangxi University, Nanning 530004, PR China*

Received 24 August 2021; accepted 19 October 2021
Available online 26 October 2021

KEYWORDS

α-MoO_3 nanobelts;
NiO;
p-n heterostructure;
Photocatalysis;
MB

Abstract In this article, Z-scheme NiO/α-MoO_3 p-n heterojunction is successfully synthesized by a facile hydrothermal route. The phase and nanostructures are researched through a series of characterizations, such as XRD, SEM, TEM, EDX, XPS and DRS. It is confirmed that the NiO nanoparticles are deposited homogeneously on one dimensional α-MoO_3 nanobelts and p-n heterojuction is constructed at the interface of α-MoO_3 and NiO. Photocatalytic activity of the as-synthesized photocatalysts is investigated by photodegradation of methylene blue (MB) under simulated solar light irradiation. Compared with bare α-MoO_3, the NiO/α-MoO_3 p-n heterojunction exhibits significantly improved photocatalytic activity and photostability for MB degradation. The improvement in the photocatalytic performance can be attributed to the optimization of the charge transport pathway offered by Z-scheme heterojunctions, which can promote the effective separation of electron-hole pairs. The results indicate that Z-scheme NiO/α-MoO_3 p-n heterojunction is a novel and efficient photocatalyst with potential application for the removal of organic contaminant in wastewater.

* Corresponding author at: Hebei Province Key Laboratory of Sustained Utilization & Development of Water Recourse, Hebei GEO University, Shijiazhuang 050031, PR China.
E-mail address: pzpzlxl@163.com (C. Lu).

Peer review under responsibility of King Saud University.

Production and hosting by Elsevier

1. Introduction

The toxic and cancerogenic organic dyes have become one of the major problems for the drinking water due to the extracts of printing, textiles and extraction mills. Confronted with the difficult degradation of multifarious organic compounds, the development and utilization of photocatalysis technology is pressing (Li et al., 2020; Wang et al., 2020; Guo et al., 2021). In the past two decades, semiconductor catalysts such as ZnO, TiO_2, Fe_2O_3, NiO, WO_3, and SnO_2 have

https://doi.org/10.1016/j.arabjc.2021.103513

attracted significant attention owing to their low toxicity, high stability and environmentally friendly (Ali et al., 2021; Yoon et al., 2021; Nguyen-Dinh et al., 2021; Rong et al., 2021). However, for the convenient and cost-efficient single-component photocatalyst, the photogenerated carriers can easily recombine, which directly causes the low quantum efficiency and poor photocatalytic activity (Dong et al., 2019; Gui et al.,2020; Dong et al.,2020; Zuo et al., 2021). Several strategies have been investigated to promote the photocatalytic performance which include element doping, noble metal functionalization, and heterostructured composite fabrication (Zhai et al., 2020; Mehmood et al., 2017; Zha et al., 2021; Li 2022). The design of new photocatalyst materials with the desired properties has become a popular research field.

α-MoO_3, a well-known n-type semiconductor, has attracted much attention on photocatalytic applications due to its unique structural and optical properties. Recently, α-MoO_3 with various morphologies and modifications have been prepared and studied (Zhang et al., 2019; Szkoda et al., 2018; Chiang et al., 2015). However, the challenge for promoting the catalytic activity of bare α-MoO_3 still exists, which mainly lies in enhancing the visible light absorption and reducing the recombination of charge carriers. In order to further degrade the adsorbed organic contaminants efficiently, α-MoO_3 has be applied in conjunction with other elements or semiconductors to form new compounds or heterojunctions. For example, Zhang et al. (Zhang et al., 2018) reported the functionalization of AuPd nanoparticles on the surface of α-MoO_3 nanowires leading to an enhanced photocatalytic activity (11.5 times higher than that of bare α-MoO_3) for the degradation of trichloroethylene. Phuruangrat et al. (Phuruangrat et al., 2016; Phuruangrat et al., 2017; Phuruangrat et al., 2016) synthesized Gd, Dy and Eu-doped α-MoO_3 nanobelts by hydrothermal method, which exhibited high visible-light-driven activity for photodegradation of MB. Feng et al. (Feng et al., 2017) combined α-MoO_3 nanobelts with AgBr to form a Z-scheme photocatalyst, resulting in the dramatic visible light absorption and improved photocatalytic performance in degrading RhB. Xi et al. (Xi et al., 2019) constructed a dye-sensitized MoO_2 incorporated α-MoO_3 photocatalyst, which displayed high RhB degradation efficiency under visible-light irradiation. Thus, it is necessary to construct the α-MoO_3-based photocatalysts to further shorten the degradation period and enhance photocatalytic efficiency.

P-n heterojunction constructed by combining a n-type semiconductor (electron-rich) with a p-type semiconductor (hole-rich) is one of the most effective methods to enhance the charge separation. Among the family of semiconductor materials, NiO, a p-type semiconductor, has been widely applied in the fabrication of p-n heterostructures with different n-type semiconductors. Up to now, a series of NiO-based composites have been studied, such as NiO/SnO_2 (Jayababu et al., 2019), TiO_2/NiO (Sun et al., 2016), NiO/Fe_2O_3 (Jana et al., 2018), ZnO/NiO (Li et al., 2018) and so on. However, to our best knowledge, there is rarely report on the preparation and photocatalytic performance of NiO/α-MoO_3 constructed p-n heterostructures. Notably, both the valence band (VB) and conduction band (CB) of NiO are more negative than those of α-MoO_3. We can introduce the appropriate band positions of NiO into α-MoO_3 to create a Z-scheme photocatalyst system, which will help decrease the electron-hole recombination of α-MoO_3 and enable us to obtain higher efficiency photocatalysts. In this work, we designed and successfully constructed a Z-scheme NiO/α-MoO_3 p-n heterojunction by a two-step hydrothermal route. The microstructure, elemental composition and optical property of the as-fabricated heterostructures were evaluated. The photocatalytic activity was estimated by using the degradation of the MB dye under simulated solar light irradiation. Finally, the possible mechanism for the photocatalytic process was proposed and discussed in detail.

2. Experimental procedures

2.1. Preparation of one dimensional α-MoO_3 nanobelts

In a typical procedure, 1.24 g of ammonium heptamolybdate tetrahydrate ($(NH_4)_6Mo_7O_{24}{\cdot}4H_2O$) was dissolved into 50 mL pure water, followed by adding 5.0 mL nitric acid (HNO_3, 65%) in a dropwise manner. After continuous stirring for 30 min, the mixture was transferred to a Teflon-lined stainless-steel autoclave with capacity of 100 mL for hydrothermal treatment at 180 °C for 36 h. Upon cooling down the autoclave to room temperature, a white precipitate was collected by filtration, washed by distilled water and ethanol, and dried at 80 °C for 24 h.

2.2. Preparation of NiO/α-MoO_3 heterostructure

NiO/α-MoO_3 heterostructures were also prepared by a hydrothermal approach. NiO/α-MoO_3 heterostructures with different mass ratios of NiO powders (1 wt%, 3 wt% and 5 wt%) were described as follows: 0.24 g of as-synthesized α-MoO_3 was suspended into 40 mL pure water with ultrasonic concussion for 20 min, and then different mass ratios of Ni$(NO_3)_2{\cdot}6H_2O$ (0.01, 0.03 and 0.05 g) and 0.4 g of D-glucose monohydrate ($C_6H_{12}O_6{\cdot}H_2O$) were put into the mixed solution under strong magnetic stirring for 15 min. Then the mixture was transferred to a 50 mL Teflon-lined stainless autoclave and heated at at 160 °C for 5 h. The product was centrifugally separated, washed several times with water/ethanol and then dried in vacuum at 70 °C for 24 h. Finally, the as-obtained materials were calcined in a muffle furnace at 400 °C for 3 h. The NiO/α-MoO_3 heterostructures with different mass ratios of NiO (1 wt%, 3 wt%, and 5 wt%) were labelled as 1% NiO/α-MoO_3, 3% NiO/α-MoO_3 and 5% NiO/α-MoO_3, respectively (EDS patterns could be seen in Fig. S1). For comparison, pure NiO was synthesised without adding of α-MoO_3 nanobelts.

2.3. Characterization

Characterization techniques are provided in the Supporting Information.

2.4. Photocatalytic activity

Photocatalytic experiments of the as-synthesized samples were examined by degrading MB in aqueous solution under simulated solar light irradiation of a 500 W Xe lamp. In a typical photocatalytic process, 0.01 g of each catalyst and 100 mL MB (10 mg L^{-1}) were added into the photocatalytic reactor. To achieve the adsorption–desorption equilibrium between the catalysts and MB dye, the solution was continuously stirred in the dark for 30 min. At periodic intervals (30 min), 2 mL of suspension was collected from the solution and separated through centrifuge to remove the photocatalyst particles. Finally, the concentration of leftover solution was analysed by the UV–vis spectrophotometer (UV-3600, Shimadzu). Recovery of photocatalyst was conducted by using methanol/acetic acid (95:5, v/v) solution. After the photocata-

lyst was contacted with the solvent completely, the photocatalyst was separated by centrifuge. To investigate the reproducibility of the photocatalyst, the photocatalyst after photocatalytic degradation was reused in experiments and the process was duplicated five times.

3. Result and discussion

The crystal structures of NiO/α-MoO_3 heterojunctions, α-MoO_3 nanobelts and NiO nanoparticles are studied by XRD analysis. As the XRD patterns revealed in Fig. 1, the diffraction peaks for bare α-MoO_3 are in accordance with JCPDS No.05–0508. The mainly characteristic peaks located in 2θ = 12.8°, 25.7° and 39.0° are indexed to (020), (040) and (060) crystal planes (Li et al., 2017), verifying the orthorhombic α-MoO_3 phase. Moreover, the pattern of NiO exhibits four diffraction peaks at about 2θ of 37.2°, 43.3°, 62.9° and 75.5°, which correspond to the crystal plane (111), (200), (220) and (311) of cubic NiO phase (JCPDS No. 47–1049) (Sun et al., 2016), respectively. It is worth to mention that all diffraction peaks of NiO/α-MoO_3 heterojunctions are matched well with the α-MoO_3 phase and no feature peaks of NiO are detected. The reason may be that there is few NiO in the nanocomposites and the diffraction peaks of α-MoO_3 can cover the NiO peaks (Li et al., 2017).

SEM, TEM and HRTEM are acquired to confirm the successful introduction of NiO nanoparticles on the α-MoO_3 nanobelts. Fig. 2(a-e) shows the typical SEM images of pure α-MoO_3, NiO/α-MoO_3 heterojunctions and NiO. The SEM results reveal that the pure α-MoO_3 material displays a belt-like structure with the length of 2–10 μm and width of 200–300 nm, and the ratio of length/width can reach as high as 50/1 (Fig. 2(a)). Pure NiO possesses a flower-like morphology with diameters ranging from 500 to 800 nm (Fig. 2(e)). Compared with pure α-MoO_3, it can be found that the surfaces of NiO/α-MoO_3 turn coarser which can be ascribed to the successful loading of the secondary NiO particles onto the α-MoO_3 substrates. However, with the increase of loading content, the independent NiO particles appear in the SEM image of 5% NiO/α-MoO_3 (Fig. 2(d)).

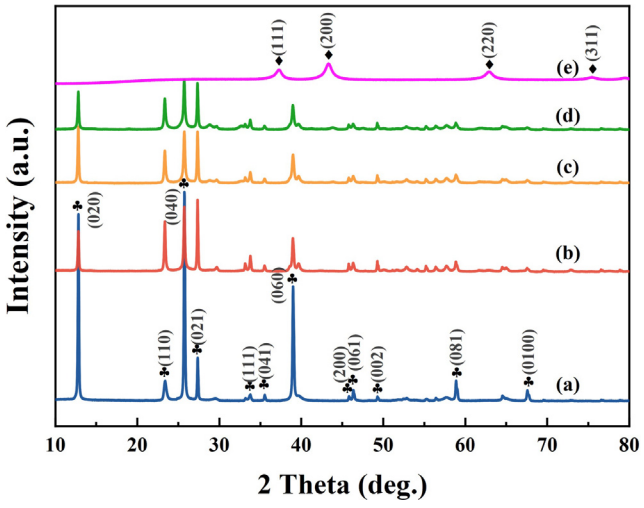

Fig. 1 XRD patterns of (a) α-MoO_3, (b) 1% NiO/α-MoO_3, (c) 3% NiO/α-MoO_3, (d) 5% NiO/α-MoO_3 and (e) NiO.

The TEM image (Fig. 2(f)) of the single NiO-functionalized α-MoO_3 nanobelt further confirms that NiO nanoparticles are uniformly dispersed on the surface of α-MoO_3 nanobelts. The HRTEM image of 3% NiO/α-MoO_3 is also acquired (Fig. 2(g)). The interplanar spacings of 0.37 nm and 0.40 nm are clearly observed, which are indexed to the (001) and (100) planes of the α-MoO_3 crystal (Li et al., 2017). As for the lattice fringe of 0.21 nm, it can be assigned to the (200) plane of NiO crystal (Hou et al., 2014; Zheng et al., 2015). The synthetic processes for the NiO/α-MoO_3 heterojunctions are illustrated in Fig. 2(h). Under the hydrothermal conditions, linear or branched oligomers are formed by the partially dehydrated glucose, which decompose into a carbon shell coating on the surface of α-MoO_3 (TGA and DSC analyses could be seen in Fig. S2). In addition, the carbon shell has distribution of –OH groups on the hydrophilic surface of α-MoO_3 (Titirici et al., 2006; Wang et al., 2015; Demir-Cakan et al., 2009). The metal nickel ions (Ni^{2+}) conjugate with the –OH groups by an electrostatic attraction or coordination effect. Some Ni^{2+} ions agglomerate together to form larger clusters with the reaction time prolonging. Finally, the NiO/α-MoO_3 heterojunctions are obtained by oxidative calcination in air to remove the carbon.

Fig. 3(a-d) illustrates the corresponding elemental mappings of Mo, O and Ni of the 3% NiO/α-MoO_3 heterojunction, which reveals the different distributions of the three elements in the heterostructure. The mapping shows that the signal of Mo is mainly displayed in the core region, and the signal of Ni is distributed from the outer layer, which further confirms that the NiO/α-MoO_3 heterojunctions are successfully obtained. Meanwhile, the EDX analysis (Fig. 3(e)) demonstrates that the elements of the heterojunctions are composed of Mo, O, and Ni and no impurities are observed. The atomic ratios for Mo and Ni are about 17:1.

XPS analysis is conducted to confirm the chemical states of the elements for 3% NiO/α-MoO_3 and pure α-MoO_3. XPS survey spectrum (Fig. 4(a)) reveals that the heterojunction mainly contains Ni, Mo and O elements, which agrees well with EDX results. Fig. 4(b) gives the XPS spectra of the Ni 2p, which reveals two edges of Ni $2p_{1/2}$ and Ni $2p_{3/2}$ (Zheng et al., 2015; Jiang et al., 2019). The Ni $2p_{3/2}$ main peak and its satellite (856.3 eV and 863.3 eV) as well as Ni $2p_{1/2}$ main peak and its satellite (873.7 eV and 880.8 eV) are ascribed to the Ni^{2+} ions in NiO, suggesting the Ni^{2+} ions are dominant in the product (Jiang et al., 2019). The Mo 3d XPS spectrum (Fig. 4(c)) exhibits two peaks at binding energies of 232.5 and 235.7 eV, which relate to Mo $3d_{5/2}$ and Mo $3d_{3/2}$ in α-MoO_3, respectively (Sunu et al., 2004; Sui et al., 2015). However, the Mo 3d peaks in NiO/α-MoO_3 heterojunctions shift to higher energies, with the binding energies of Mo $3d_{5/2}$ and Mo $3d_{3/2}$ shifting to 232.9 and 236.1 eV, respectively. The Gauss fitting curves of the O 1s spectra (Fig. 4(d)) of pure α-MoO_3 and 3% NiO/α-MoO_3 contain two peaks centered at 530.6/531.0 eV and 532.1/532.5 eV, which come from the lattice oxygen in α-MoO_3 and chemisorbed oxygen site (Li et al., 2017; Yang et al.,2017), respectively. It is obvious that the O 1s binding energy peaks of 3% NiO/α-MoO_3 show a shift to higher value. The slight variation of Mo or O electronic structure may be attributed to the formation of heterojunction interface between two phases which would play a critical role in the photocatalytic process of the heterojunctions.

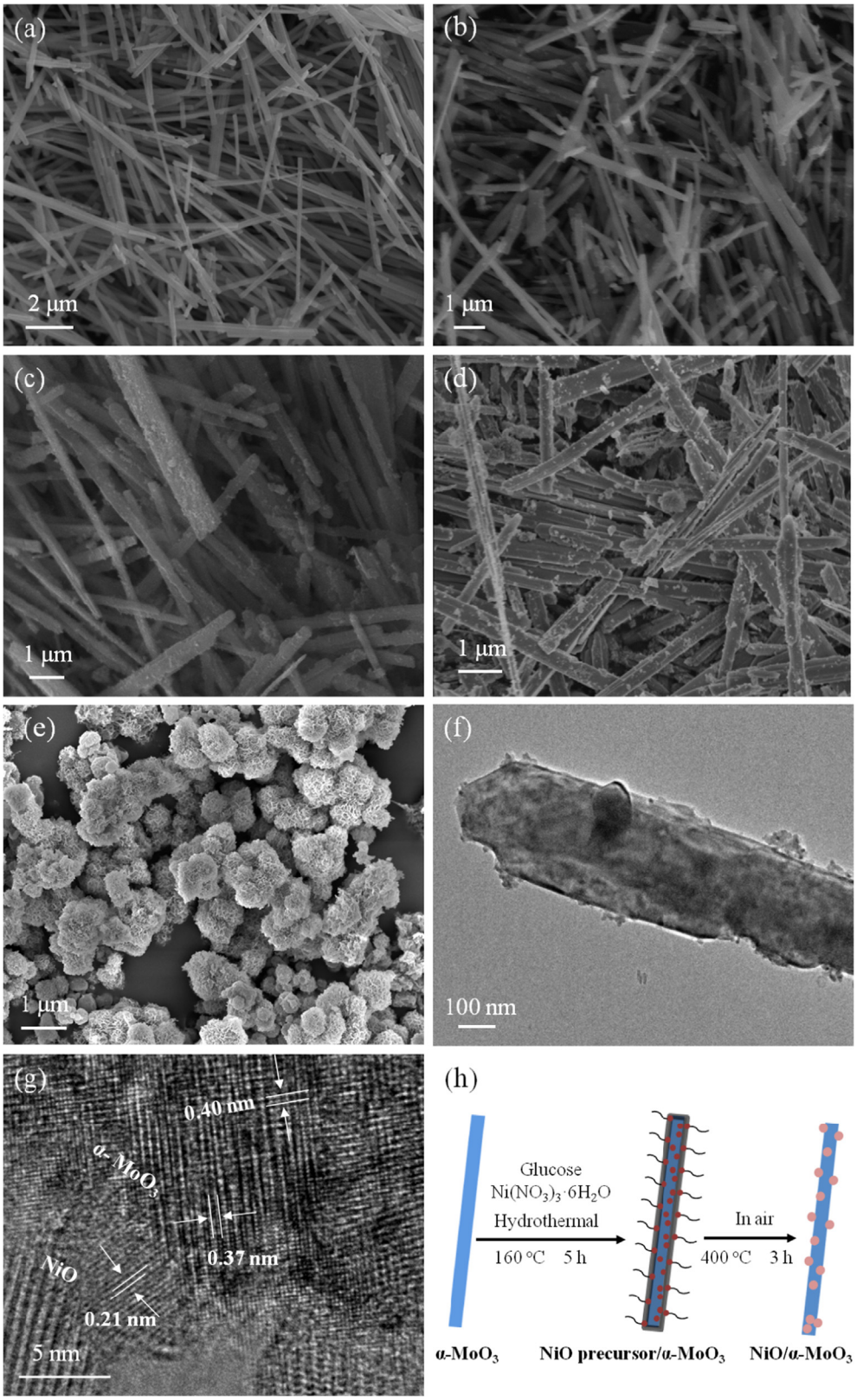

Fig. 2 SEM images of (a) α-MoO_3, (b) 1% NiO/α-MoO_3, (c) 3% NiO/α-MoO_3, (d) 5% NiO/α-MoO_3 and (e) NiO; TEM (f) and HRTEM (g) images of 3% NiO/α-MoO_3; (h) Schematic illustration for the preparation of the NiO/α-MoO_3 heterojunctions.

The optical absorption properties of α-MoO_3, NiO and a series of NiO/α-MoO_3 heterojunctions are investigated by UV–Vis diffuse reflectance spectroscopy (DRS) in Fig. 5(a). The bare NiO has a pronounced light absorption in the wavelength region 200–800 nm because of its dark color (Li et al., 2021; Sabzehparvar et al., 2021). While for pure α-MoO_3, it

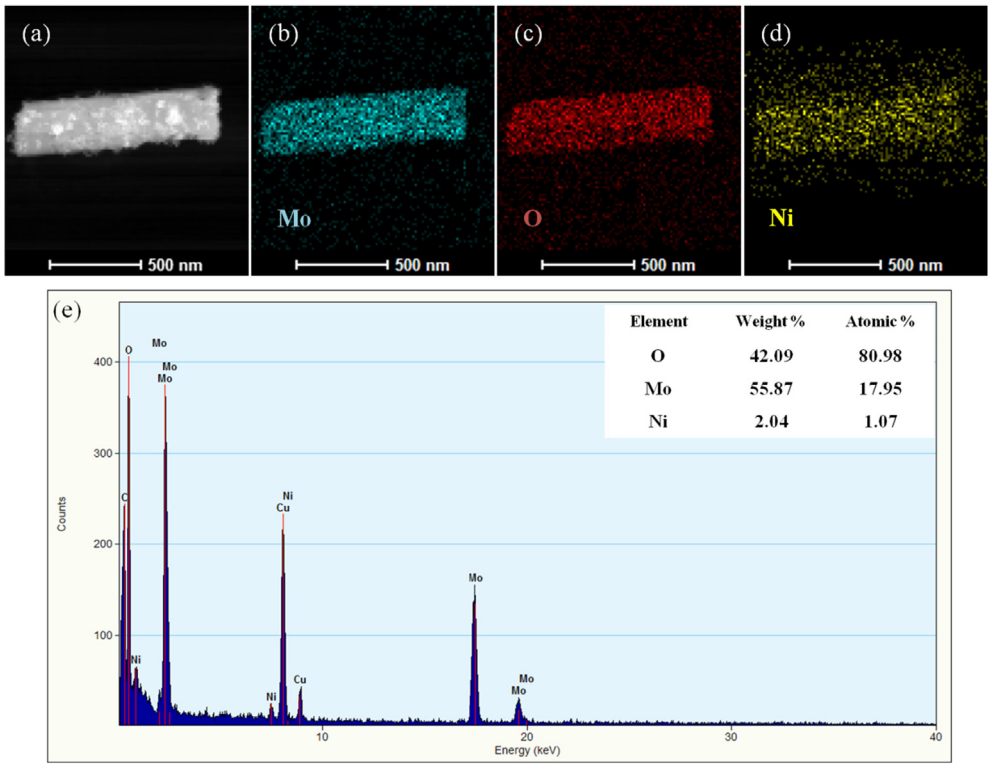

Fig. 3 The scanning TEM image (a) and corresponding elemental mappings (b-d) of Mo, O, and Ni of 3% NiO/α-MoO_3 heterojunctions, respectively; EDX image (e) of the heterojunctions.

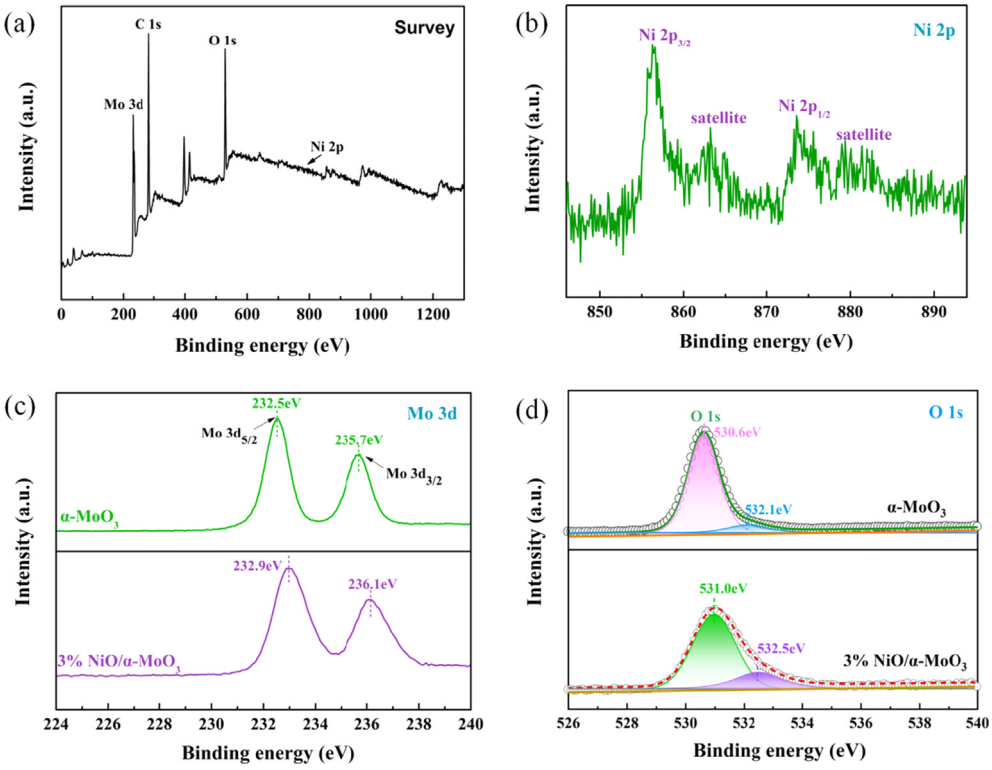

Fig. 4 Full survey scan spectra (a) and Ni 2p XPS spectra (b) of 3% NiO/α-MoO_3 heterojunction; high-resolution XPS spectra of Mo 3d (c) and O 1s (d) of bare α-MoO_3 and 3% NiO/α-MoO_3 heterojunction.

displays a steep absorption edge at 420 nm and exhibits the intrinsic absorption in UV region and the weak absorption band in visible wavelength. By contrast, the absorption edge of the composites shows an obvious shift towards the visible range upon decoration of NiO, which might be caused by the strong interactions between α-MoO_3 and NiO of the heterostructure (Sabzehparvar et al., 2021). The red shift of the absorption wavelengths is favorable for the NiO/α-MoO_3 heterojunctions to absorb light in the broader region and enhance the visible light photoresponse. The optical band gap can be calculated according to the Tauc equation: $(\alpha hv)^2 = A\ (hv\text{-}Eg)$. As shown in Fig. 5(b), the estimated band gaps of α-MoO_3 and NiO by the plot of $(\alpha hv)^2$ vs. hν are 3.25 and 3.08 eV (vs. NHE), respectively, which are identical with the previous studies (Sun et al., 2016; Li et al., 2017). To further get the band position of pure α-MoO_3 and NiO, XPS valence band spectra is employed to investigate the VB energy levels. As shown in Fig. 5(c), the maximum energy edges of VB density of states for pure α-MoO_3 and NiO are approximately at 3.27 eV and 0.53 eV (vs. NHE), respectively. Furthermore, the position of CB is calculated according to the formula: $Eg = E_{VB} - E_{CB}$. Thus, the CB values of α-MoO_3 and NiO are calculated to be 0.02 and −2.55 eV, respectively. According to the above computed results, the energy-levels of the semiconductors are worked out in Fig. 5(d). It reveals that the VB and CB positions of NiO are negative than those of α-MoO_3, demonstrating the suitable energy band structures for them to construct the heterostructure composites.

The photocatalytic activities of as-prepared samples are investigated by the MB photodegradation under simulated solar light irradiation. Fig. 6(a) shows the photodegradation efficiency of the photocatalysts. Obviously, for the blank experimental analysis, it can be seen that MB is hardly degraded under visible and catalyst-free conditions, which fully shows that MB is very stable in the aqueous solution. The MB removal efficiency of pure α-MoO_3 and NiO is only 41.3% and 49.8% in 2 h, respectively, implying the poor degradation efficiency of the pristine samples. While, after the addition of different amount of NiO, the photocatalytic performance is significantly enhanced. The photoactivity of the NiO/α-MoO_3 heterojunctions follows the order of 3% NiO/α-MoO_3 > 5% NiO/α-MoO_3 > 1% NiO/α-MoO_3, with the removal efficiency of 96.5%, 77.4% and 66.5%, respectively. The results show that 3% NiO/α-MoO_3 exhibits the best photocatalytic performance, and the MB is almost completely degraded after 2 h of light irradiation (Fig. 6(b)). The reaction kinetics of the MB degradation by different photocatalysts is fitted to a first order model and Fig. 6(c) displays the plot between $Ln(C_0/C)$ and reaction time. The corresponding apparent rate constants of the catalysts for MB degradation are 0.00375, 0.00515, 0.00903, 0.02685 and 0.01143 min^{-1}, respectively (Fig. 6(d)). Noticeably, the k value for MB degradation over 3% NiO/α-MoO_3 (0.02685 min^{-1}) is 7.16 folds than that of bare α-MoO_3 (0.00375 min^{-1}). To verify the universality of our catalysts, we selected some other organic contaminants, such as RhB and phenol, for photocatalytic degradation over 3% NiO/α-MoO_3. As exhibited in Fig. S3, 3% NiO/α-MoO_3 exhibits good photocatalytic activity towards other organic contaminants.

In addition to photodegradation efficiency, the photostability of the catalysts is also a very significant factor for practical applications. In order to evaluate the photostability and degradation rate for 3% NiO/α-MoO_3 heterojunction, the cycling runs in the MB degradation are carried out. Fig. 7

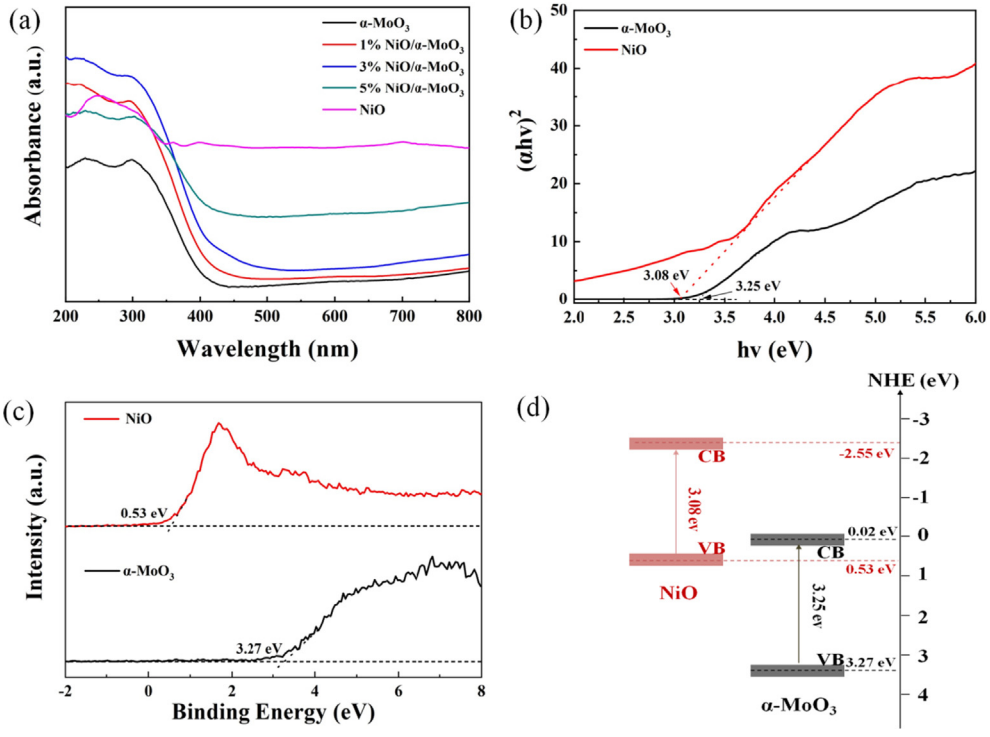

Fig. 5 (a) UV–vis DRS of α-MoO_3, NiO and a series of NiO/α-MoO_3 heterojunctions; (b) Eg values of α-MoO_3 and NiO; (c) XPS valence band spectrum for α-MoO_3 and NiO. (d) The band structure diagrams of α-MoO_3 and NiO.

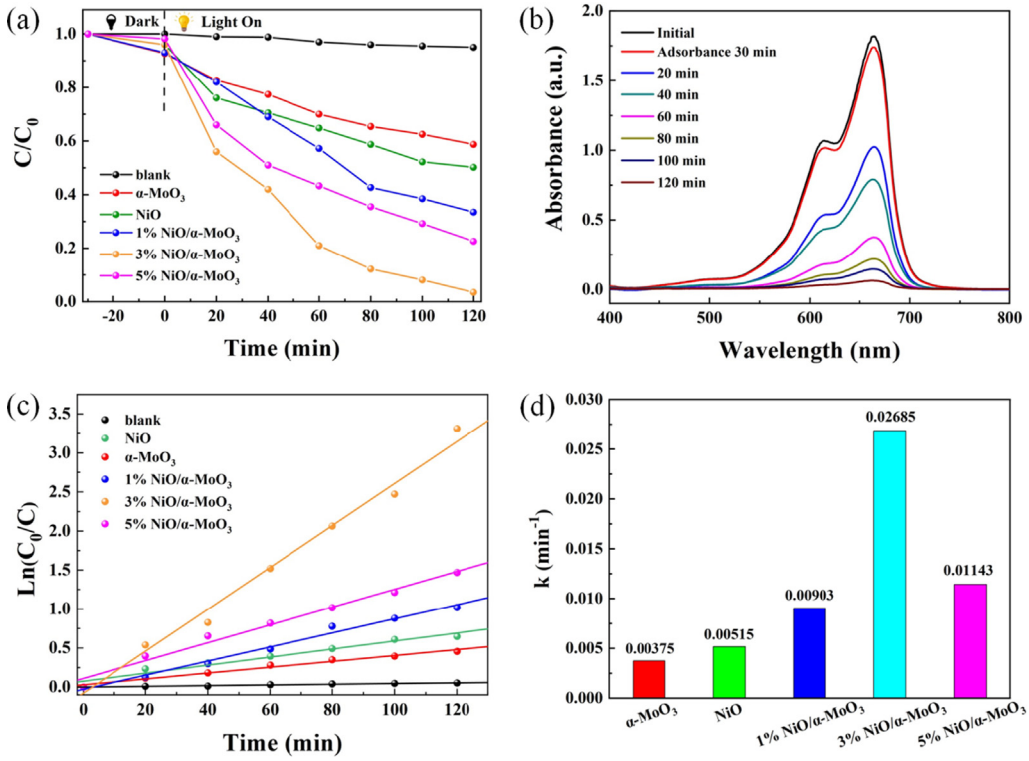

Fig. 6 (a) Photodegradation efficiency of MB over various photocatalysts; (b) Absorption spectra of MB with time using 3% NiO/α-MoO_3; (c) The pseudo-first-order reaction kinetics and (d) apparent rate constants of the photocatalysts for MB degradation.

(a) displays that the photocatalytic degradation rate of 3% NiO/α-MoO_3 heterojunction is retained at 94.3% after five successive experimental runs, confirming that 3% NiO/α-MoO_3 heterojunction is very stable during the photocatalytic degradation processes. No apparent crystalline structure and morphology's changes are observed in the XRD pattern (Fig. 7(b)) and SEM image (Fig. S4) of 3% NiO/α-MoO_3 after cyclicing experiment, which further demonstrates the significant stability of the photocatalyst. Furthermore, when compared with other reports for photodegradation of MB (Table S1), this work displays better photocatalytic degradation rate constant. Therefore, it can be inferred that the 3% NiO/α-MoO_3 heterojunction is a reusable photocatalyst for application in treatment of organic pollutants from wastewaters.

Nitrogen adsorption–desorption isotherm curves of as-prepared photocatalysts are shown in Fig. 8(a). It can be seen that the loading of NiO nanoparticles on α-MoO_3 nanobelts results in an enhancement of specific surface area (13.32 m^2 g^{-1}) in comparison with pristine α-MoO_3 (7.34 m^2 g^{-1}). The heterojunction with the higher surface area can provide more active sites, thus improve the adsorption capacity and photocatalytic degradation activities (Shi et al.,2020). To investigate the influence of NiO introduction on the behavior of charge carriers, several photo-electrochemical measurements including PL, photocurrent response measurement and EIS are car-

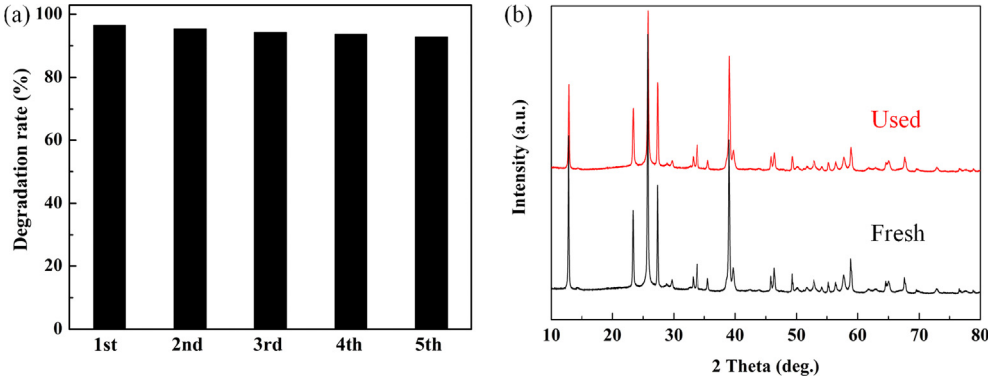

Fig. 7 (a) Cycling runs of 3% NiO/α-MoO_3 heterojunction for photodegradation of MB; (b) XRD patterns of 3% NiO/α-MoO_3 before and after 5 runs.

ried out to reveal the intrinsic charge separation characteristics. In Fig. 8(b), PL spectra is displayed to probe the photogenerated electron transfer of the α-MoO_3 and 3% NiO/α-MoO_3 heterojunction. Pristine α-MoO_3 has a strong emission peak centered at 460 nm, which possesses the strongest PL emission intensity. After the loading of NiO, the PL emission intensity of 3% NiO/α-MoO_3 exhibits a rapid decrease compared with the pure α-MoO_3. Ordinarily, a weaker PL intensity implies a lower recombination rate of photoinduced electron-hole pairs (Guo et al., 2021; Wang et al., 2021). Thus, the decoration of NiO can provide more electron-hole capture sites, which leads to enhanced photocatalytic activity. The transient photocurrent response spectra of 3% NiO/α-MoO_3 and bare α-MoO_3 are recorded for four intermittent light on–off circulations in Fig. 8(c). The pure α-MoO_3 has a poor light current response of about 0.01 μA/cm^2, while the photocurrent response of 3% NiO/α-MoO_3 is much higher at about 0.04 μA/cm^2. This indicates the faster transfer rate of photogenerated electrons of 3% NiO/α-MoO_3 heterojunction, leading to a more efficient carriers transfer process (Zhang et al., 2021; Zhou et al., 2021). Moreover, the EIS Nyquist plots of the photocatalysts are exhibited in Fig. 8(d) and 3% NiO/α-MoO_3 heterojunction shows the smaller arc radius than bare α-MoO_3. The result further indicates that the heterojunction possesses a lower charge-transfer resistance and thus a faster charge-transfer rate in the photodegradation process (Lu et al., 2019).

For the purpose of explore the main reactive species of 3% NiO/α-MoO_3 during MB photodegradation, the trapping experiments are implemented with ethylenediamine tetraacetate (EDTA-2Na) as the hole (h^+) scavenger, benzoquinone (BQ) as the superoxide radical ($\bullet O_2^-$) scavenger and isopropanol (IPA) as the hydroxyl (•OH) scavenger. As displayed in Fig. 9(a), when no scavenger is added in the system, the degradation rate of 3% NiO/α-MoO_3 is still 96.5% within 120 min. In contrast, when EDTA-2Na, BQ and IPA are added, the degradation rate is significantly restrained, indicating that h^+, $\bullet O_2^-$ and •OH are all the key active species in the photodegradation process. Spintrapping ESR technology is conducted to further verify the $\bullet O_2^-$ and •OH generated in the photocatalytic processes. The ESR signals of 3% NiO/α-MoO_3 under xenon lamp irradiation and in the dark are presented in Fig. 9(b). No characteristic peaks of active species can be observed under dark conditions. However, six clear signals of $\bullet O_2^-$ appear under xenon lamp irradiation, which proves the presence of $\bullet O_2^-$ in the photodegradation process over 3% NiO/α-MoO_3 heterojunction photocatalyst. Moreover, when 3% NiO/α-MoO_3 heterojunction is irradiated under xenon lamp, four characteristic signals of •OH with intensity of 1:2:2:1 are detected. The ESR results reveal that both $\bullet O_2^-$ and •OH are involved, and they can play important roles in decomposing MB dye (Li et al., 2020).

Considering the experimental results described above and the calculated band gap structures, the proposed mechanism of NiO/α-MoO_3 heterojunction under light irradiation is presented in Fig. 10. Due to the well-matched VB and CB positions, a heterojunction can form between α-MoO_3 and NiO, and two possible mechanisms are proposed: (a) traditional heterojunction-type II and (b) Z-scheme type. The CB and VB potentials of NiO (−2.55 eV vs. NHE and 0.53 eV vs. NHE) are more negative than those of α-MoO_3 (0.02 eV vs. NHE and 3.27 eV vs. NHE, respectively). If the charge transfer

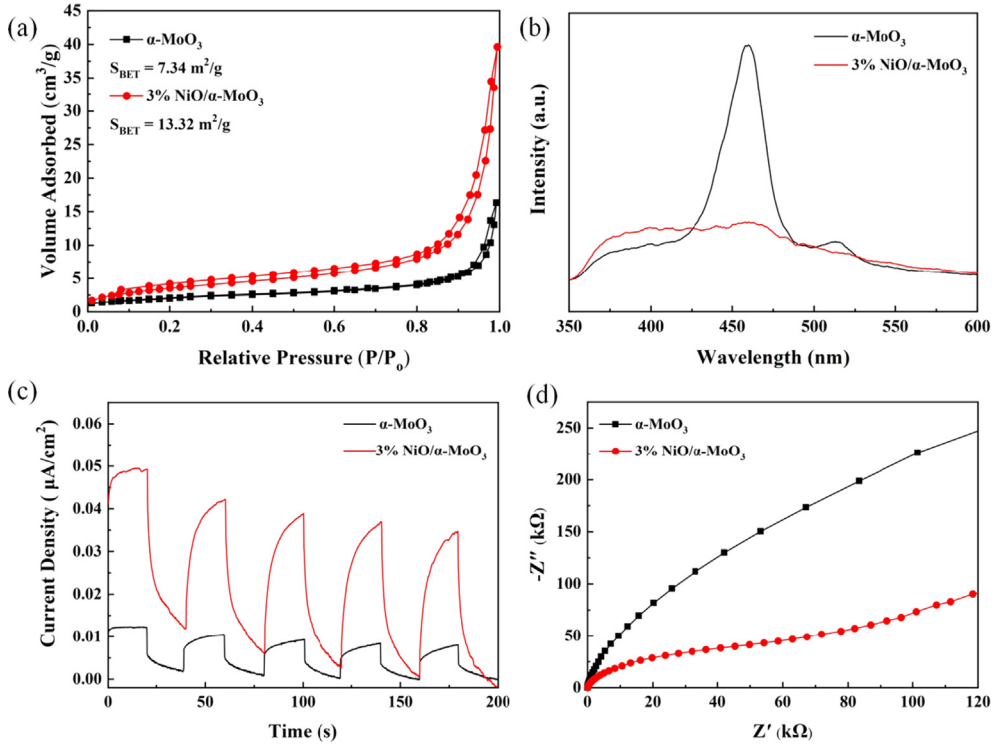

Fig. 8 (a) Nitrogen adsorption–desorption isotherms, (b) PL spectra, (c) transient photocurrent responses and (d) EIS Nyquist spectra of bare α-MoO_3 and 3% NiO/α-MoO_3 heterojunction.

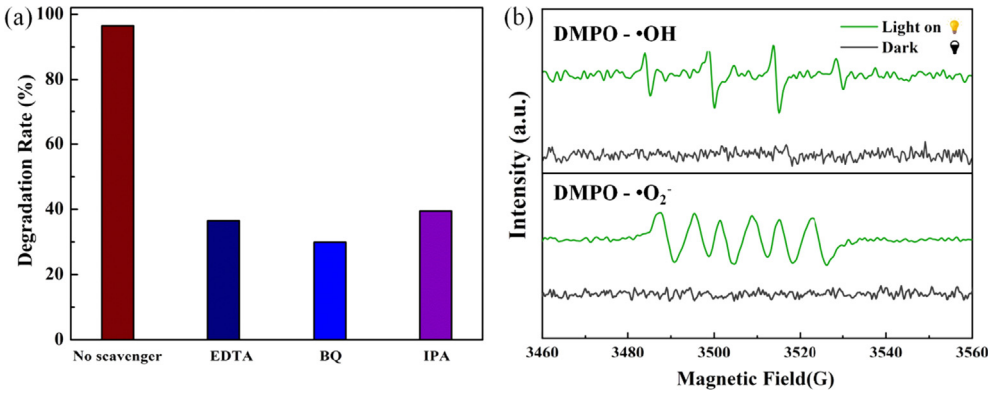

Fig. 9 (a) Active species trapping experiments of MB degradation over 3% NiO/α-MoO_3; (b) ESR spectra of 3% NiO/α-MoO_3 heterojunction: DMPO- •O_2^- in methanol dispersion and DMPO- •OH in aqueous dispersion.

route follows the traditional type-II mechanism in Fig. 10(a), the electrons in the CB of NiO will transform to the CB of α-MoO_3 and holes in the VB of α-MoO_3 move to the VB of NiO. Consequently, the electrons will accumulate on the CB of α-MoO_3, and the holes will accumulate on the VB of NiO. However, the system may not have high reduction potential (only 0.02 eV for CB of α-MoO_3) and oxidation potential (only 0.53 eV for VB of NiO) for generating •O^{2-} (−0.33 eV) and •OH radicals (1.99 and 2.74 eV) (Li et al., 2020; Zeng et al., 2021). This presumption is contradictory to the ESR results, in which •O^{2-} and •OH are detected to be the main active species during the photodegradation process. Thus, it is supposed that a more reasonable Z-scheme photoelectron migration emerges in the p-n heterojunction.

NiO is a p-type material, and the Fermi level is close to the VB; α-MoO_3 is a n-type material, and the Fermi level is near to the CB (Teng et al.,2017; Sun et al., 2016; Zhao et al.,2021; Wang et al., 2020). As shown in Fig. 10(b), E_F of NiO is higher than that of α-MoO_3. After contact of NiO with α-MoO_3, electrons will transfer from NiO to α-MoO_3 until unified E_F is fabricated. At the equilibrium state, NiO loses electrons and is positively charged; while α-MoO_3 acquires electrons and forms an electron-rich layer (Xu et al., 2019). This process forms an internal electric field at the interface and induces energy band bending (Deng et al., 2021). When NiO/α-MoO_3 p-n heterojunction is irradiated by the simulated sunlight, the photoinduced electrons at the CB of α-MoO_3 will rapidly transfer to the VB of NiO and recombine with the photoexcited holes at the VB of NiO. Therefore, the corresponding photogenerated electrons and holes are left at the CB of NiO and the VB of α-MoO_3, respectively, which retains the high oxidation and reduction capabilities of the NiO/α-MoO_3. Meanwhile, useless photogenerated electrons (from the CB of α-MoO_3) and holes (from the VB of NiO) are consumed relatively, and useful charge carriers are preserved effectively through the intimate heterojunction interface, which can be sufficiently derived in the photocatalytic system (Li et al., 2019). Therefore, •O_2^- and •OH should be the main active species in the reaction and degrade MB, which was consistent with the result of ESR. This Z-scheme heterojunction not only effectively promote the separation of photogenerated charges, but also retain the prominent redox potential (Muñoz-Batista et al., 2016; Zheng et al., 2019).

4. Conclusions

In summary, the Z-scheme NiO/α-MoO_3 p-n heterojunction has been prepared through a two-step hydrothermal route. And the decoration of NiO is demonstrated to be a promising approach to design highly active and stable α-MoO_3 based photocatalysts. According to the SEM/TEM/EDX/XPS analysis, the NiO nanoparticles are successfully grown on α-MoO_3 nanobelts, forming heterojuction at the interface of

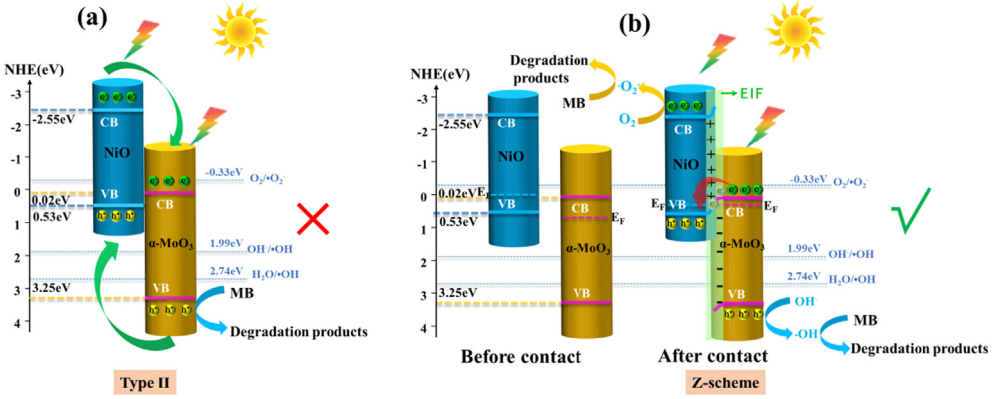

Fig. 10 Two models of charge migration for NiO/α-MoO_3 p-n heterojunction: (a) traditional heterojunction-type II (b) and Z-scheme type.

NiO and α-MoO_3. Compared with pure α-MoO_3 nanoblets, the NiO/α-MoO_3 heterojunction exhibits enhanced photocatalytic activity, achieving 96.5% photocatalytic efficiency within 2 h under simulated solar light irradiation. Meanwhile, the heterostructures retain relatively consistent activity after five repeat cycles. A Z-scheme charge transfer process between NiO and α-MoO_3 can be inferred, which significantly accelerates the charge separation. This study provides a reference for the future research of MoO_3-based p-n heterojunction photocatalysts.

Declaration of Competing Interest

The authors declare that they have no known competing financial interests or personal relationships that could have appeared to influence the work reported in this paper.

Acknowledgements

This work is supported by the National Natural Science Foundation of China (21906039), Hebei Province 333 Talents Project (A202101020), Funding Project for Introduced Overseas Scholars of Hebei Province (C20190321), Science and Technology Project of Hebei Education Department (BJ2021010), Doctoral research fund of Hebei Geo University (BQ2019041), Funding for basic scientific research of universities in Hebei Province and Funding for the Science and Technology Innovation Team Project of Hebei GEO University (KJCXTD-2021-02).

Appendix A. Supplementary material

Supplementary data to this article can be found online at https://doi.org/10.1016/j.arabjc.2021.103513.

References

Ali, A., Shoeb, M., Li, Y., Li, B.A., Khan, M.A., 2021. Enhanced photocatalytic degradation of antibiotic drug and dye pollutants by graphene-ordered mesoporous silica (SBA 15)/TiO_2 nanocomposite under visible-light irradiation. J. Mol. Liq. 324,. https://doi.org/10.1016/j.molliq.2020.114696 114696.

Chiang, T.H., Ho, P.Y., Chiu, S.Y., Chao, A.C., 2015. Synthesis, characterizationand photocatalytic activity of α-MoO_3 particles utilizing different polyol monomers under visible light irradiation. J. Alloy. Compd. 651, 106–113. https://doi.org/10.1016/j.jallcom.2015.08.091.

Demir-Cakan, R., Baccile, N., Antonietti, M., Titirici, M.M., 2009. Carboxylate-richcarbonaceous materials via one-step hydrothermal carbonization of glucose in the presence of acrylic acid. Chem. Mater. 21, 484–490. https://doi.org/10.1021/cm802141h.

Deng, H.Z., Fei, X.G., Yang, Y., Fan, J.J., Yu, J.G., Cheng, B., Zhang, L.Y., 2021. S-scheme heterojunction based on p-type $ZnMn_2O_4$ and n-type ZnO with improved photocatalytic CO_2 reduction activity. Chem. Eng. J. 409,. https://doi.org/10.1016/j.cej.2020.127377 127377.

Dong, S.Y., Cui, L.F., Liu, C.Y., Zhang, F.Y., Li, K.Y., Xia, L.J., Su, X.F., Feng, J.L., Zhu, Y.F., Sun, J.H., 2019. Fabrication of 3D ultra-light graphene aerogel/Bi_2WO_6 composite with excellent photocatalytic performance: a promising photocatalysts for water purification. J. Taiwan Inst. Chem. Eng. 97, 288–296. https://doi.org/10.1016/j.jtice.2019.02.016.

Dong, S.Y., Cui, L.F., Zhang, W., Xia, L.J., Zhou, S.J., Russell, K.C., Fan, M.H., Feng, J.L., Sun, J.H., 2020. Double-shelled $ZnSnO_3$ hollow cubes for efficient photocatalytic degradation of antibiotic wastewater. Chem. Eng. J. 384. https://doi.org/10.1016/j.cej.2019.123279.

Feng, B., Wu, Z.Y., Liu, J.S., Zhu, K.J., Li, Z.Q., Jin, X., Hou, Y.d., Xi, Q.Y., Cong, M.Q., Liu, P.C., Gu, Q.L., 2017. Combination of ultrafast dye-sensitized-assisted electron transfer process and novel Z-scheme system: AgBr nanoparticle interspersed MoO_3 nanobelts for enhancing photocatalytic performance of RhB. Appl. Catal. B-Environ. 206, 242–251. https://doi.org/10.1016/j.apcatb.2017.01.029.

Gui, L., Chen, Z., Chen, B.Y., Song, Y.Z., Yu, Q., Zhu, W., Hu, Q., Liu, Y.Y., Zheng, Z.Y., Lv, Z., You, H.J., Yeasmin, F., 2020. Preparation and characterization of ZnO/PEG-Co(II)-PbO_2 nanocomposite electrode and an investigation of the electrocatalytic degradation of phenol. J. Hazard. Mater. 399,. https://doi.org/10.1016/j.jhazmat.2020.123018 123018.

Guo, F., Huang, X.L., Chen, Z.H., Cao, L.W., Cheng, X.F., Chen, L.Z., Shi, W.L., 2021a. Construction of Cu_3P-$ZnSnO_3$-g-C_3N_4 p-n-n heterojunction with multiple built-in electric fields for effectively boosting visible-light photocatalytic degradation of broad-spectrum antibiotics. Sep. Purif. Technol. 265,. https://doi.org/10.1016/j.seppur.2021.118477 118477.

Guo, F., Huang, X.L., Chen, Z.H., Shi, Y.X., Sun, H.R., Cheng, X.F., Shi, W.L., Chen, L.Z., 2021b. Formation of unique hollow $ZnSnO_3$@$ZnIn_2S_4$ core-shell heterojunction to boost visible-light-driven photocatalytic water splitting for hydrogen production. J. Colloid Interface Sci. 602, 889–897. https://doi.org/10.1016/j.jcis.2021.06.074.

Hou, S.C., Zhang, G.H., Zeng, W., Zhu, J., Gong, F.L., Li, F., Duan, H.G., 2014. Hierarchical core-shell structure of ZnO Nanorod@-NiO/MoO_2 composite nanosheet arrays for high-performance supercapacitors. ACS Appl. Mater. Interfaces 6 (16), 13564–13570. https://doi.org/10.1021/am5028154.

Jana, S., Mondal, A., Ghosh, A., 2018. Fabrication of stable NiO/Fe_2O_3 heterostructure: A versatile hybrid material for electrochemical sensing of glucose, methanol and enhanced photodecomposition and/photoreduction of water contaminants. Appl. Catal. B-Environ. 232, 26–36. https://doi.org/10.1016/j.apcatb.2018.03.038.

Jayababu, N., Poloju, M., Shruthi, J., Reddy, M., 2019. Semi shield driven p-n heterostructures and their role in enhancing the room temperature ethanol gas sensing performance of NiO/SnO_2 nanocomposites. Ceram. Int. 45, 15134–15142. https://doi.org/10.1016/j.ceramint.2019.04.255.

Jiang, W.H., Meng, L.L., Zhang, S.F., Chuai, X.H., Zhou, Z.J., Hu, C.H., Sun, P., Liu, F.M., Yan, X., Lu, G.Y., 2019. Design of highly sensitive and selective xylene gas sensor based on Ni-doped MoO_3 nano-pompon. Sensor. Actuat. B-Chem. 299,. https://doi.org/10.1016/j.snb.2019.126888 126888.

Li, H.P., Ba, G.M., Liang, Z.W., Deng, Q.H., Hou, W.G., 2019. Construction of direct all-solid-state Z-scheme *p-n* copper indium disulfide/tungsten oxide heterojunction photocatalysts: function of interfacial electric field. J. Colloid. Interf. Sci. 555, 72–81. https://doi.org/10.1016/j.jcis.2019.07.073.

Li, J.B., Yan, D., Hou, S.J., Lu, T., Yao, Y.F., Chua, D.H.C., Pan, L.K., 2018. Metal-organic frameworks derived yolk-shell ZnO/NiO microspheres as high-performance anode materials for lithium-ion batteries. Chem. Eng. J. 335, 579–589. https://doi.org/10.1016/j.cej.2017.10.183.

Li, J.T., Liu, H.J., Fu, H., Xu, L., Jin, H., Zhang, X.W., Wang, L.W., Yu, K.F., 2017a. Synthesis of 1D α-MoO_3/0D ZnO heterostructure nanobelts with enhanced gas sensing properties. J. Alloy. Compd. 788, 248–256. https://doi.org/10.1016/j.jallcom.2019.02.086.

Li, J.T., Wang, L.W., Liu, H.J., Zhao, J., Li, X., Wei, H., Han, Y.F., 2017b. Synthesis and enhanced toluene gas sensing properties of 1-D α-MoO_3/$Fe_2(MoO_4)_3$ heterostructure. J Alloy Compd. 694, 939–945. https://doi.org/10.1016/j.jallcom.2016.10.142.

Li, N., Li, Y.M., Zhou, Y.J., Li, W.J., Ji, S.D., Yao, H.L., Cao, X., Jin, P., 2017c. Interfacial-charge-transfer-induced photochromism of MoO_3@TiO_2 crystalline-core amorphous-shell nanorods. Sol.

Energ. Mat. Sol. C. 160, 116–125. https://doi.org/10.1016/j.solmat.2016.10.016.

Li, S.J., Chen, J.L., Hu, S.W., Jiang, W., Liu, Y.P., Liu, J.S., 2020. A novel 3D Z-scheme heterojunction photocatalyst: $Ag_6Si_2O_7$ anchored on flower-like Bi_2WO_6 and its excellent photocatalytic performance for the degradation of toxic pharmaceutical antibiotics. Inorg. Chem. Front. 7, 529–541. https://doi.org/10.1039/C9QI01201J.

Li, S.J.*, Wang, C.C., Cai, M.J., Yang, F., Liu, Y.P., Chen, J.L., Zhang, P., Li, X.*, 2022. Facile fabrication of TaON/Bi_2MoO_6 core–shell S-scheme heterojunction nanofibers for boosting visible-light catalytic levofloxacin degradation and Cr(VI) reduction, Chem. Eng. J. 428, 131158. 10.1016/j.cej.2021.131158.

Li, S.Y., Tang, Y.W., Wang, M., Kang, J., Jin, C.Y., Liu, J.Y., Li, Z. L., Zhu, J.W., 2021. NiO/g-C_3N_4 2D/2D heterojunction catalyst as efficient peroxymonosulfate activators toward tetracycline degradation: Characterization, performance and mechanism. J. Alloy. Compd. 880,. https://doi.org/10.1016/j.jallcom.2021.160547 160547.

Lu, C.Y., Guo, F., Yan, Q.Z., Zhang, Z.J., Li, D., Wang, L.P., Zhou, Y.H., 2019. Hydrothermal synthesis of type II $ZnIn_2S_4$/$BiPO_4$ heterojunction photocatalyst with dandelion-like microflower structure for enhanced photocatalytic degradation of tetracycline under simulated solar light. J. Alloy. Compd. 811,. https://doi.org/10.1016/j.jallcom.2019.151976 151976.

Mehmood, F., Iqbal, J., Jan, T., Mansoor, Q., 2017. Structural, Raman and photoluminescence properties of Fe doped WO_3 nanoplates with anticancer and visible light driven photocatalytic activities. J. Alloy. Compd. 728, 1329–1337. https://doi.org/10.1016/j.jallcom.2017.08.234.

Muñoz-Batista, M.J., Fontelles-Carceller, O., Ferrer, M., Fernández-García, M., AnnaKubacka, 2016. Disinfection capability of Ag/g-C_3N_4 composite photocatalysts under UV and visible light illumination. Appl. Catal. B: Environ. 183, 86–95. https://doi.org/10.1016/j.apcatb.2015.10.024.

Nguyen-Dinh, M.T., Bui, T.S., Bansal, P., Jourshabani, M., Lee, B.K., 2021. Photocatalytic and photo-electrochemical behavior of novel SnO_2-modified-g-C_3N_4 forcomplete elimination of tetracycline under visible-light irradiation: Slurry and fixed-bed approach. Sep. Purif. Technol. 267,. https://doi.org/10.1016/j.seppur.2021.118607 118607.

Phuruangrat, A., Cheed-Im, U., Thongtem, T., Thongtem, S., 2016a. High visible light photocatalytic activity of Eu-doped MoO_3 nanobelts synthesized by hydrothermal method. Mater. Lett. 172, 166–170. https://doi.org/10.1016/j.matlet.2016.02.141.

Phuruangrat, A., Thipkonglas, S., Thongtem, T., Thongtem, S., 2017. Hydrothermalsynthesis and characterization of Dy-doped MoO_3 nanobelts for using as a visible-light-driven photocatalyst. Mater. Lett. 195, 37–40. https://doi.org/10.1016/j.matlet.2017.02.053.

Phuruangrat, A., Im, U.C., Thongtem, T., Thongtem, S., 2016b. Influence of Gd dopant on photocatalytic properties of MoO_3 nanobelts. Mater. Lett. 173, 158–161. https://doi.org/10.1016/j.matlet.2016.03.018.

Rong, R., Wang, L.M., 2021. Synthesis of hierarchical hollow nest-like WO_3 micro/nanostructures with enhanced visible light-driven photocatalytic activity. J. Allo.y Compd. 850,. https://doi.org/10.1016/j.jallcom.2020.156742 156742.

Sabzehparvar, M., Kiani, F., Tabrizi, N.S., 2021. Mesoporous-assembled TiO_2-NiO-Ag nanocomposites with p-n/Schottky heterojunctions for enhanced photocatalytic performance. J. Alloy. Compd. 876,. https://doi.org/10.1016/j.jallcom.2021.160133 160133.

Shi, W.L., Li, M.Y., Huang, X.L., Ren, H.J., Guo, F., Tang, Y.B., Lu, C.Y., 2020. Construction of $CuBi_2O_4$/Bi_2MoO_6 p-n heterojunction with nanosheets-onmicrorods structure for improved photocatalytic activity towards broadspectrum antibiotics degradation. Chem. Eng. J. 394,. https://doi.org/10.1016/j.cej.2020.125009 125009.

Sui, L.L., Xu, Y.M., Zhang, X.F., Cheng, X.L., Gao, S., Zhao, H., Cai, Z., Huo, L.H., 2015. Construction of three-dimensional flower-like α-MoO_3 with hierarchical structure for highly selective triethylamine sensor. Sensor. Actuat. B-Chem. 208, 406–414. https://doi.org/10.1016/j.snb.2014.10.138.

Sun, B., Zhou, G.W., Gao, T.T., Zhang, H.J., Yu, H.H., 2016. NiO nanosheet/TiO_2 nanorod-constructed p-n heterostructures for improved photocatalytic activity. Appl. Surf. Sci. 364, 322–331. https://doi.org/10.1016/j.apsusc.2015.12.158.

Sunu, S.S., Prabhu, E., Jayaraman, V., Gnanasekar, K.I., Seshagiri, T. K., Gnanasekaran, T., 2004. Electrical conductivity and gas sensing properties of MoO_3. Sens. Actuators B Chem. 101, 161–174. https://doi.org/10.1016/j.snb.2004.02.048.

Szkoda, M., Trzciński, K., Klein, M., Siuzdak, K., Oleksiak, A.L., 2018. The influence of photointercalaction and photochromism effects on the photocatalytic properties of electrochemically obtained maze-like MoO_3 microstructures. Sep. Purif. Technol. 197, 382–387. https://doi.org/10.1016/j.seppur.2018.01.033.

Teng, W., Tan, X.J., Li, X.Y., Tang, Y.B., 2017. Novel Ag_3PO_4/MoO_3 p-n heterojunction with enhanced photocatalytic activity and stability under visible light irradiation. Appl. Surf. Sci. 409, 250–260. https://doi.org/10.1016/j.apsusc.2017.03.025.

Titirici, M.M., Markus, Antonietti A., Thomas, A., 2006. A generalized synthesis of metal oxide hollow spheres using a hydrothermal approach. Chem. Mater. 18, 3808–3812. https://doi.org/10.1021/cm052768u.

Wang, L.P., Huang, T.T., Yang, G.P., Lu*, C.Y., Dong, F.L., Li, Y. L., Guan*, W.S., 2020a. The precursor-guided hydrothermal synthesis of $CuBi_2O_4$/WO_3 heterostructure with enhanced photoactivity under simulated solar light irradiation and mechanism insight. J. Hazard. Mater. 381, 120956–120967. https://doi.org/10.1016/j.jhazmat.2019.120956.

Wang, Q., Sun, J., Wang, Q., Zhang, D.A., Xing, L.L., Xue, X.Y., 2015. Electrochemical performance of α-MoO_3-In_2O_3 core-shell nanorods as anode materials forlithium-ion batteries. J. Mater. Chem. A. 3, 5083–5091. https://doi.org/10.1039/C5TA00127G.

Wang, S.H., Zhao, L., Huang, W., Zhao, H., Chen, J.Y., Cai, Q., Jiang, X., Lu, C.Y., Shi, W.L., 2021. Solvothermal synthesis of CoO/$BiVO_4$ p-n heterojunction withmicro-nano spherical structure for enhanced visible light photocatalytic activity towards degradation of tetracycline. Mater. Res. Bull. 135,. https://doi.org/10.1016/j.materresbull.2020.111161 111161.

Wang, Z.H., Zhang, K.C., Fei, T., Gu, F.B., Han, Dongmei, 2020b. α-Fe_2O_3/NiO heterojunction nanorods with enhanced gas sensing performance for acetone. Sens. Actuators, B 318,. https://doi.org/10.1016/j.snb.2020.128191 128191.

Xi, Q.Y., Liu, J.S., Wu, Z.Y., Bi, H.F., Li, Z.Q., Zhu, K.J., Zhuang, J. J., Chen, J.X., Lu, S.L., Huang, Y.F., Qian, G.M., 2019. In-situ fabrication of MoO_3 nanobelts decorated with MoO_2 nanoparticles and their enhanced photocatalytic performance, App.l Surf. Sci. 480, 427–437. https://doi.org/10.1016/j.apsusc.2019.03.009.

Xu, Q.L., Ma, D.K., Yang, S.B., Tian, Z.F., Cheng, B., Fan, J.J., 2019. Novel g-C_3N_4/g-C_3N_4 S-scheme isotype heterojunction for improved photocatalytic hydrogengeneration. Appl. Surf. Sci. 495,. https://doi.org/10.1016/j.apsusc.2019.143555 143555.

Yang, S., Liu, Y.L., Chen, T., Jin, W., Yang, T.Q., Cao, M.C., Liu, S. S., Zhou, J., Zakharova, G.S., Chen, W., 2017. Zn doped MoO_3 nanobelts and the enhanced gas sensing properties to ethanol. Appl. Surf. Sci. 393, 377–384. https://doi.org/10.1016/j.apsusc.2016.10.021.

Yoon, J., Oh, S.G., 2021. Synthesis of amine modified ZnO nanoparticles and their photocatalytic activities in micellar solutions under UV irradiation. J. Ind. Eng. Chem. 96, 390–396. https://doi.org/10.1016/j.jiec.2021.01.043.

Zeng, Z.L., Jing, D.W., Guo, L.J., 2021. Efficient hydrogen production in a spotlight reactor with plate photocatalyst of TiO_2/NiO heterojunction supported on nickel foam. Energy. 228,. https://doi.org/10.1016/j.energy.2021.120578 120578.

Zha, R.H., Shi, T., He, L., Zhang, M., 2021. Synergetic excitonic and defective effects in confined SnO_2/α-Fe_2O_3 nanoheterojunctions for efficient photocatalytic molecular oxygen activation. Chem. Eng. J. 421,. https://doi.org/10.1016/j.cej.2021.129883 129883.

Zhai, H.S., Liu, X.L., Wang, Z.Y., Liu, Y.Y., Zheng, Z.K., Qin, X.Y., Zhang, X.Y., Wang, P., Huang, B.B., 2020. ZnO nanorod decorated by Au-Ag alloy with greatly increased activity for photocatalytic ethylene oxidation. Chinese. J. Catal. 41, 1613–1621. https://doi.org/10.1016/S1872-2067(19)63473-X.

Zhang, W.Q., Shi, W.L., Sun, H.R., Shi, Y.X., Luo, H., Jing, S.R., Fan, Y.Q., Guo, F., Lu, C.Y., 2021. Fabrication of ternary CoO/g-C_3N_4/Co_3O_4 nanocomposite with p-n-p type heterojunction for boosted visible-light. J. Chem. Technol. Biotechnol. 96, 1854–1863. https://doi.org/10.1002/jctb.6703.

Zhang, X.N., Yi, J.J., Chen, H.X., Mao, M., Liu, L., She, X.J., Ji, H. Y., Wu, X.Y., Yuan, S.Q., Xu, H., Li, H.M., 2019. Construction of a few-layer g-C_3N_4/α-MoO_3 nanoneedles all-solid-state Z-scheme photocatalytic system for photocatalytic degradation. J. Energy. Chem. 29, 65–71. https://doi.org/10.1016/j.jechem.2018.

Zhang, Y.F., Park, S.J., 2018. Bimetallic AuPd alloy nanoparticles deposited on MoO_3 nanowires for enhanced visible-light driven trichloroethylene degradation. J. Catal. 361, 238–247. https://doi.org/10.1016/j.jcat.2018.03.010.

Zhao, H., Li, C.F., Liu, L.Y., Palma, B., Hu, Z.Y., Renneckar, S., Larter, S., Li, Y., Kibria, M.G., Hu, J.G., Su, B.L., 2021. n-p Heterojunction of TiO_2-NiO core-shell structure for efficient hydrogen generation and lignin photoreforming. J. Colloid Interface Sci. 585, 694–704. https://doi.org/10.1016/j.jcis.2020.10.049.

Zheng, X., Yan, X.Q., Sun, Y.H., Bai, Z.M., Zhang, G.J., Shen, Y.W., Liang, Q.J., Zhang, Y., 2015. Au-Embedded ZnO/NiO hybrid with excellent electrochemical performance as advanced electrode materials for supercapacitor. ACS Appl. Mater. Interfaces. 7, 2480–2485. https://doi.org/10.1021/am5073468.

Zheng, X.T., Yang, L.M., Li, Y.B., Yang, L.X., Luo, S.L., 2019. Direct Z-scheme $MoSe_2$ decorating TiO_2 nanotube arrays photocatalyst for water decontamination. Electrochim. Acta 298, 663–669. https://doi.org/10.1016/j.electacta.2018.12.130.

Zhou, L.P., Dai, S.Q., Xu, S., She, Y.Q., Li, Y.L., Leveneur, S., Qin, Y.L., 2021. Piezoelectric effect synergistically enhances the performance of Ti_{32}-oxo-cluster/$BaTiO_3$/CuS p-n heterojunction photocatalytic degradation of pollutants. Appl. Catal. B-Environ. 291,. https://doi.org/10.1016/j.apcatb.2021.120019 120019.

Zuo, G.C., Wang, Y.T., Wei, L.T., Xian, Q.M., Zhao, Y.L., 2021. Direct Z-scheme TiO_2-$ZnIn_2S_4$ nanoflowers for cocatalyst-free photocatalytic water splitting. Appl. Catal. B 291,. https://doi.org/10.1016/j.apcatb.2021.120126 120126.